Rock Mechanics Bulletin 5 (2026) 100316

Contents lists available at ScienceDirect

Rock Mechanics Bulletin

journal homepage: www.keaipublishing.com/en/journals/rock-mechanics-bulletin

From CT scans to surface metrics: A novel workflow for rock fracture roughness evaluation at sample scale

Elisa Mammoliti[a], Alessia Caputo[b,*], Maria Teresa Calcagni[b], Giovanni Salerno[b], Paolo Castellini[b]

[a] Department of Science and Engineering of Matter, Environment and Urban Planning, Polytechnic University of Marche, via Brecce Bianche, Ancona, 60131, Italy
[b] Department of Industrial Engineering and Mathematical Sciences, Polytechnic University of Marche, via Brecce Bianche, Ancona, 60131, Italy

ARTICLE INFO

Keywords:
Fracture roughness characterization
3D X-Ray tomography
Digital microscope topography
Convolutional neural network
Barton comb profilometer

ABSTRACT

This study presents a robust deep learning-based workflow for fracture segmentation and subsequent Joint Roughness Coefficient computation from X-ray computed tomography data. The core of the approach is a convolutional neural network trained on a heterogeneous multi-material fracture dataset, capable of accurately segmenting even sub-millimetric and low-contrast features without domain-specific retraining. This network demonstrated superior continuity, robustness, and precision compared with classical image-processing approaches, identifying a higher number of fractures and providing a more complete representation of the fracture network. In the proposed workflow, the convolutional neural network output is converted into a high-resolution three-dimensional point cloud, from which surface roughness is computed directly using the widely adopted Joint Roughness Coefficient metric. The method is validated against: (i) point clouds derived from high-resolution digital microscope images, and (ii) digitized profiles acquired with the Barton comb profilometer. This multi-method validation captures microscale roughness variability and ensures robustness across different acquisition modalities. The results confirm that the CNN-based CT workflow provides a non-destructive, scalable, and objective solution for fracture roughness characterization, particularly suitable for intact core samples and inaccessible discontinuities.

1. Introduction

Fracture roughness generally refers to the geometrical irregularity of a discontinuity surface relative to its mean plane (Brady and Brown, 2006) comprising both small-scale unevenness and large-scale waviness (Bieniawski and Hawkes, 1978). Traditionally, roughness is estimated using contact or non-contact profilometric techniques, including mechanical stylus profilometers (Brown et al., 1986; Glover et al., 1998), laser profilometry (Xie et al., 1999), digital photogrammetry, shadow methods, or structured light scanning (Ge et al., 2014; Salvini et al., 2020; López-Torres et al., 2020). Among field-based approaches, Barton comb profilometer (Barton and Choubey, 1977) is widely adopted, allowing empirical correlation between profile morphology and the Joint Roughness Coefficient (JRC), which remains one of the most widely used parameters in rock mechanics to estimate the peak shear strength, especially in the Barton model, where it influences the frictional behavior of discontinuities. In practice, JRC is most commonly assessed by visually comparing the joint profiles with a set of ten standard reference profiles with values ranging from 0 to 20 (Barton and Choubey, 1977; International Society for Rock Mechanics, 1981). While standardized, this method is intrinsically subjective, as it depends on the operator's ability to match the joint surface to the reference profiles. Most existing methods for joint roughness characterization rely on surface accessibility and subjective assessment (Barton and Choubey, 1977; International Society for Rock Mechanics, 1981), which limits their applicability in cases involving internal or sealed fractures, such as those found in intact core samples (Brown et al., 1986; Xie et al., 1999; Ge et al., 2014). Furthermore, these techniques are often manual, lack automation, and are not easily scalable to large datasets (Tse and Cruden, 1979; Salvini et al., 2020). Recent advances in non-contact roughness acquisition—such as photogrammetry and laser scanning—have significantly improved spatial resolution and field applicability (Salvini et al., 2020). However, they still require direct access and a clear line-of-sight to the joint surface, making them unsuitable for

* Corresponding author.
E-mail address: a.caputo@pm.univpm.it (A. Caputo).
Peer review under the responsibility of Chinese Society for Rock Mechanics & Engineering.

https://doi.org/10.1016/j.rockmb.2026.100316
Received 7 August 2025; Received in revised form 19 December 2025; Accepted 9 February 2026
Available online 28 February 2026

analyzing internal or sealed fractures within intact rock cores. This underscores the need for non-destructive methods capable of resolving roughness characteristics in inaccessible features. To overcome this limitation, several researchers have proposed quantitative approaches for JRC estimation based on mathematical descriptors of surface topography. Early methods relied on statistical indicators derived from 1D profiles—such as root mean square slope or structure functions—but these have shown sensitivity to sampling intervals and profile orientation (Tse and Cruden, 1979). More recently, 3D techniques such as photogrammetry and laser scanning have emerged, offering improved spatial coverage and resolution. Nonetheless, a persistent challenge remains: all these surface-based techniques still require physical access to the fracture plane, which precludes their application to internal discontinuities in core samples without destructive intervention. This further emphasizes the growing need for non-invasive methods that can characterize closed joints embedded within the rock mass. In this context, 3D X-ray computed tomography (CT) presents a compelling solution. CT imaging enables high-resolution, non-destructive internal visualization of fracture networks, allowing for the analysis of roughness and morphological features even in sealed or inaccessible fractures. Previous studies have demonstrated that CT-based methods can characterize internal discontinuities with precision comparable to surface-based approaches (Diaz et al., 2017), while also preserving the specimen and supporting analyses under realistic boundary conditions. While CT offers substantial advantages, a major challenge in its application is the accurate segmentation of narrow, sub-parallel fractures from the surrounding matrix. This difficulty arises from the Partial Volume Effect and the inherent low contrast of microfractures, which can lead to underestimation or misclassification of features (Ketcham and Carlson, 2001; Ketcham, 2006; Ketcham et al., 2010). To overcome these limitations, this study introduces a physically validated digital workflow that combines deep learning-based segmentation of fracture networks from CT data with automated surface roughness quantification. In previous research Caputo et al. (2025) some of these techniques have been evaluated with these CT data, but their use is more complex and not automated due to parameter selection. This is why in this study, we adopt a neural network approach in particular a convolutional neural network (CNN) to extract the fracture network from 2D CT data of a calcareous rock sample. The network enables accurate identification of internal fractures, producing a high-resolution point cloud (3 million points with 70.69×10^{-3} mm) suitable for geometric analysis. JRC is computed from the 3D point cloud by applying the equation from Diaz et al. (2017), enabling a fully non-destructive, quantitative assessment of fracture morphology. A convolutional neural network (CNN) has been adopted to extract the fracture network from 2D CT data of a calcareous rock sample. In recent years, CNN-based architectures have been increasingly applied for fracture detection in geological materials due to their ability to capture complex morphological patterns and outperform classical image processing techniques in terms of segmentation accuracy and generalization (Chen et al., 2021; Tian et al., 2025; Vu and Jardani, 2022; Lei and Fan, 2024; Alzubaidi et al., 2021; Zvarivadza et al., 2025; Guo et al., 2025). For instance, Yaqoob et al. (2024) proposed a large annotated dataset for fracture edge detection in geological outcrops, demonstrating the capability of U-Net-based models to achieve high accuracy in segmenting discontinuities. Similarly, Alzubaidi et al. (2023) developed a two-stage segmentation approach for drill-core images, highlighting the advantages of deep learning in resolving fine and poorly contrasted fractures, while Pham et al. (2023) introduced an ensemble deep learning strategy for characterizing fractures in CT images of rocks, reporting robust performance even under challenging imaging conditions. For example, Guo et al. (2025) successfully employed U-Net architectures to extract cracks from CT data of fractured sandstone to establish constitutive models, while Zvarivadza et al. (2025) demonstrated the high accuracy of deep learning in rock mass classification tasks. However, while these studies demonstrate the efficacy of CNNs, they predominantly rely on training models exclusively on geological datasets similar to the target application. The CNN adopted in this study was instead trained on a curated, high-resolution dataset including fractures from a broad range of materials and structural contexts. This cross-domain training strategy enabled the network to learn diverse morphological patterns based on shape and contrast rather than specific texture, achieving robust generalization across heterogeneous materials. This allows for reliable segmentation even of sub-millimetric and low-contrast features—conditions that remain particularly challenging in conventional CT-based analyses.

This study expands upon previous work (Caputo et al., 2025), where the segmentation performance of the same architecture was benchmarked against classical image-processing techniques, demonstrating improved continuity, robustness, and precision in fracture detection tasks. In particular, compared to the alternative algorithm tested in that study, the network identified a higher number of fractures, including fine and poorly contrasted ones, thus providing a more comprehensive and accurate representation of the fracture network. In the present workflow, the output of the CNN segmentation is converted into a high-resolution three-dimensional point cloud (3 million points with 70.69×10^{-3} mm spacing), which forms the basis for quantitative analysis of surface morphology. JRC is computed directly from the extracted geometry using the method described by Diaz et al. (2017), enabling a fully digital and repeatable estimation of roughness without requiring physical access to the fracture surface. Roughness measurements derived from tomography are validated using (i) high-resolution imaging obtained with a digital microscope, and (ii) direct contact measurements based on Barton comb profilometer. In the latter case, characteristic Barton's JRC profiles were digitized for calculating the JRC according to Li and Zhang equations (Li and Zhang, 2015). This dual validation framework, based on both imaging and tactile reference standards, ensures the robustness of the proposed method, particularly in the context of intact core samples where destructive analysis is not feasible.

2. Methods

2.1. Geological setting and sample description

The sample selected for this study was collected from the Maiolica geological formation (Fm., upper Tithonian–lower Aptian), in the Valleremita area, (Umbria-Marche stratigraphic succession, Northern Apennines, Fig. 1a). The sample contains two dominant open joints without any infilling material (Fig. 1b and c), numerous calcite-filled veins—some of which show evidence of partial dissolution—and minor tectonic stylolites with clay mineral infill. According to Invernizzi, (1994), the presence of clay minerals likely contributed to the development of both stylolites and cleavage during compressional phases of the Apennine orogeny. The veins, which primarily consist of fibrous calcite, formed as extensional features resulting from fluid migration and mineral precipitation within pre-existing fractures (Bons, 2000). From a geological perspective, the fracture pattern of the sample is the result of multiple tectonic events (Centamore et al., 1971) of the Apennines. During the Late Triassic to Early Jurassic, the area was part of an extensive carbonate platform that underwent fragmentation due to Early Jurassic rifting. This tectonic activity created structural highs and lows, where pelagic sediments were predominantly deposited in the lower-lying areas. Continued subsidence during the Late Jurassic facilitated the widespread accumulation of calcareous pelagic sediments. From the Cretaceous through the Oligocene, extensional processes resulted in significant variations in sediment thickness and structural configuration (Cello et al., 1997; Marchegiani et al., 1999). The collision between the Adria microplate and the Eurasian plate in the Oligocene was instrumental in forming the Apennine orogenic belt (Calamita and Deiana, 1986; Deiana and Pialli, 1994). Subsequently, Miocene turbidites filled the basin, followed by Pliocene to Pleistocene sandstones and mudstones. Present-day tectonics are characterized by NW–SE oriented

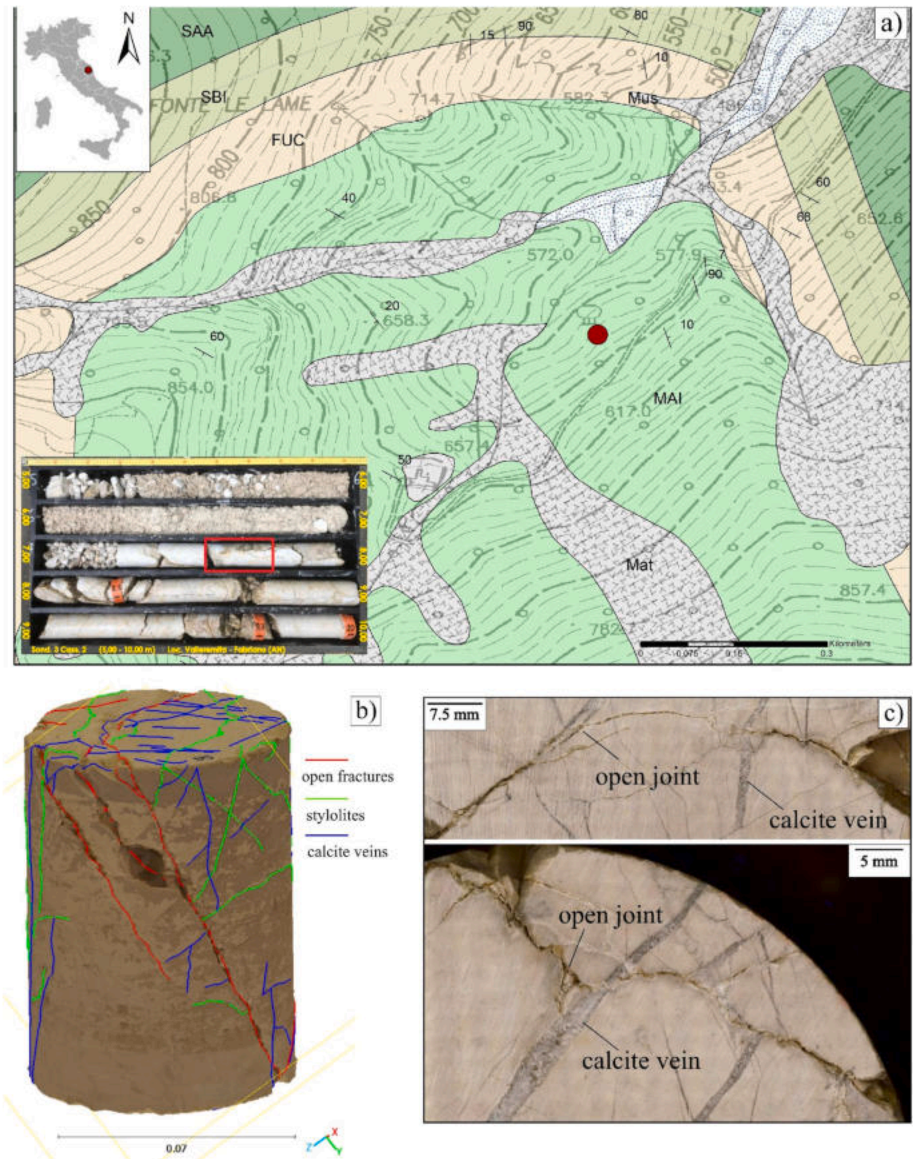

Fig. 1. Geological framework and sample locations: (a) geological map with sample location (red dot). Mat: Matelica synthem; MAI: Maiolica Fm.; FUC: Marne a Fucoidi Fm.; SBI: Scaglia Bianca Fm.; SAA: Scaglia Rossa Fm.; VAS: Scaglia Variegata Fm. (b) 3D photogrammetric model with discretization of discontinuity types; (c) high-resolution details of sample discontinuities.

normal faulting indicative of an extensional stress regime.

2.2. 3D X-ray tomography

The methodology employed in this study relies on X-ray computed tomography (CT), a non-destructive imaging technique that captures internal density variations of objects by analyzing their response to X-ray exposure (International Organization for Standardization, 2017). For this purpose, a Zeiss Metrotom 1500 system (Gmb, 2015) was used, featuring a scanning volume of up to 350 mm in all spatial directions (x, y, z). The system operates with a fixed tube-to-detector distance of 1500 mm and allows for positional adjustments along the X-axis between the source and the sample holder. This configuration makes it possible to modify the voxel size, achieving resolutions as fine as 5 μm by reducing the source-to-object distance, an important factor for resolving fine-scale features (Kruth et al., 2011). To maintain the sample's stability during scanning, a custom mounting system was adopted, ensuring accurate alignment with the X-ray beam and minimizing movement artifacts (Fig. 2). The acquisition of tomographic data involves two main stages: scanning and reconstruction. During the scanning phase, the X-ray source emits a cone-shaped beam that passes through the sample and is then captured by the detector as a series of grayscale projections. These images reflect the material-specific attenuation of X-rays and provide information about the internal structure. The sample is rotated incrementally through a full 360°, allowing image acquisition from numerous angles (Chiffre et al., 2014). The reconstruction phase uses these projections to compute a detailed 3D model of the scanned object.

After the data acquisition, the next step involves the reconstruction phase. During this phase, the multiple two-dimensional projections collected throughout the scanning process are processed and merged to create a precise three-dimensional model that represents the internal structure and density distribution of the sample. For the specific analysis conducted in this study, the total scanning time was approximately 1.5 h, influenced by an image averaging setting of 3, which extended the overall duration. The resulting reconstructed volume had a spatial resolution of 70.69 μm, with the final voxel matrix comprising 1495 × 1553 × 1770 voxels, providing a highly detailed volumetric representation of the sample.

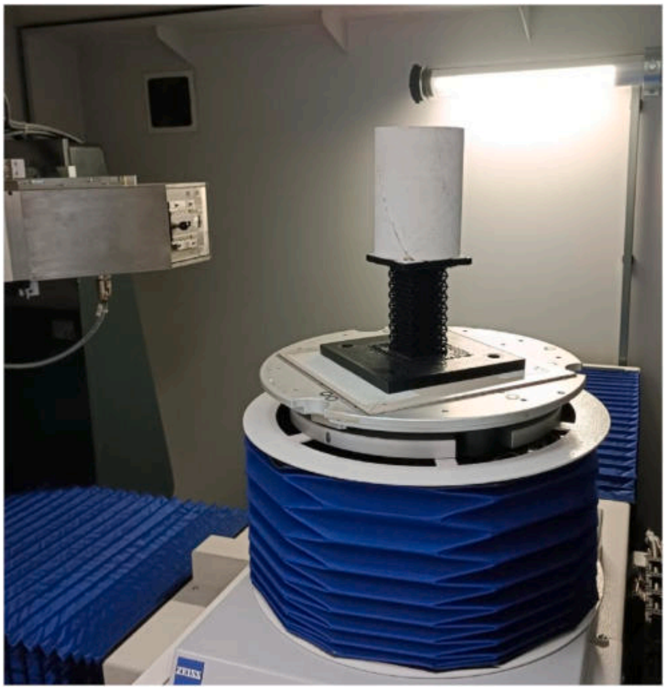

Fig. 2. Sample mounted in the Metrotom 1500 Tomograph.

2.2.1. 3D fracture network extraction

The specimen analyzed in this study has a cylindrical shape and was positioned inside the tomograph with its main axis aligned vertically. Although this setup deviates from common tomographic best practices, which typically advise against symmetrical positioning to avoid confusion between actual specimen symmetries and those introduced by reconstruction algorithms, it was considered suitable here due to the specific focus on fractures, which do not exhibit such symmetry. Placing the cylinder vertically also facilitated the interpretation and processing of the results. For each tomographic slice, the circular cross-section of the specimen was identified to enable precise masking and alignment across layers. An average image was then computed from the aligned slices, representing the specimen's internal density distribution primarily along the radial direction. Analysis of the tomographic data revealed density variations caused by several factors.

- natural heterogeneities within the specimen, such as inclusions of different materials
- systematic artifacts generated by the reconstruction algorithm, which affect all slices uniformly
- air-filled cracks that cause localized drops in density.

To highlight density fluctuations related to fractures, the average density image was subtracted from each individual slice, thus minimizing the effects of intrinsic heterogeneities and reconstruction artifacts. Each slice was given as input to the UNet neural network architecture to extrapolate and identify cracks in the material of interest. UNet is a type of fully convolutional network (FCN) originally designed for the segmentation of biomedical images, introduced by Olaf Ronneberger and colleagues (Ronneberger et al., 2015). It is particularly suited for semantic segmentation tasks and is characterised by a symmetric encoder-decoder structure. The encoding (contraction) path comprises repeated applications of two 3×3 convolutional layers followed by a rectified linear unit (ReLU) and a 2×2 max pooling operation, which downsamples the spatial resolution. At each downsampling step, the number of feature channels is doubled to increase the network representation capacity. The decoding (expansion) path mirrors the encoder one, beginning with an upsampling of the feature maps, followed by a transposed convolution that halves the number of feature channels. The output is then concatenated with a feature map clipped from the corresponding layer in the encoder. This is followed by two more 3×3 convolutions, each of which is followed by a ReLU activation. The final layer applies a 1×1 convolution to project each 64-dimensional feature vector onto the desired number of classes. Although initially developed for the medical sector, UNet has proven to be very effective in a wide range of segmentation applications, especially in scenarios with limited annotated data. For instance, Chen et al. used the UNet model to create an automatic bridge failure detector (Chen et al., 2023), while Salerno et al. adapted it for crack detection in masonry structures, demonstrating its versatility beyond biomedical use (Salerno et al., 2024; Giulietti et al., 2023). In this case, the model was trained using a dataset of 750 manually segmented images (divided into training, validation, and testing with percentages of 80:10:10%) of cracks in masonry and concrete taken in the field and online, to improve the model's generalisation ability and avoid (or reduce) overfitting. In fact, the model has already been successfully tested in various applications and could also give satisfactory results on other types of surfaces with fissures, Calcagni et al. (2025). Training was carried out over 130 epochs and lasted 1-2 h using an NVIDIA GeForce RTX 4090 GPU. Once the segmentation masks were obtained from the U-Net model, a structured post-processing pipeline was applied to move from mask data to fracture identification. In fact, the aim of this research was to convert the UNet output (masks) into a high-resolution three-dimensional point cloud that starts the basis for quantitative analysis of the considered surfaces. The binary masks were first smoothed to reduce high-frequency noise and improve the consistency of the detected structures, an essential step to improve the reliability of the subsequent steps. After smoothing, connected component labelling was used to identify regions of contiguous voxels associated with fractures, a visual representation of the process is shown in Fig. 3. The labeled regions were converted into a 3D point cloud, with each point representing a voxel identified as part of a fracture within the volume. To facilitate spatial analysis of the fracture geometry, the point cloud was mapped into a three-dimensional coordinate system. A clustering algorithm based on Euclidean distance - specifically the MATLAB built-in function pcsegdist - was then applied. This approach enables the separation of individual fracture surfaces, even in areas where discontinuities intersect, ensuring that each surface can be analyzed independently for roughness quantification. The algorithm groups points that lie within a predefined spatial threshold, effectively isolating geometrically distinct clusters. This step is crucial for delineating individual fracture surfaces or segments and supports a more refined structural analysis of their spatial distribution and morphology. The coordinates of the detected fractures were aggregated into point clouds that represent the fracture locations. Finally, the point cloud was clustered to group points belonging to the same fracture, eliminate noise points, and separate distinct cracks for subsequent geometric analyses.

2.2.2. Roughness calculation from 3D X-ray tomography data

Open fracture roughness was assessed by estimating the JRC using height-based statistical descriptors derived from fracture surface profiles. Roughness was calculated in selected regions for all the fractures identified in the 3D fracture network model. Following the method proposed by Diaz et al. (2017), each fracture surface was reoriented so that its average plane coincided with the XY plane. Specifically, the reference plane was determined by applying a least square fitting procedure to the fracture point cloud, thereby defining the best-fit plane to the overall surface. This plane was then aligned with the XY plane to provide a consistent reference for roughness measurements. This transformation allows for enhanced visualization and analysis of topographic features. The projected area, along with the vertical relief (R_z), defined as the distance between the highest peak (Z_{max}) and the lowest valley (Z_{min}), was calculated for each segment. In our method, the surface roughness was characterized by extracting a series of five evenly spaced parallel planes (Fig. 4). These five profiles were spaced at 5 mm

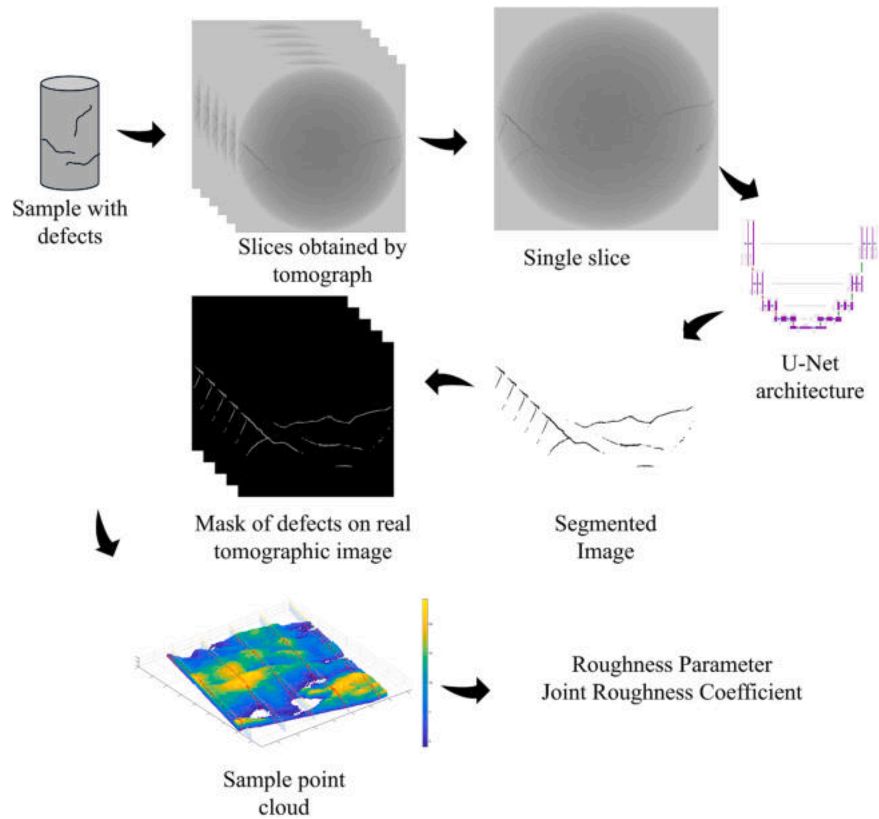

Fig. 3. Slice processed by U-Net Neural Network to extract fractures from material of interest.

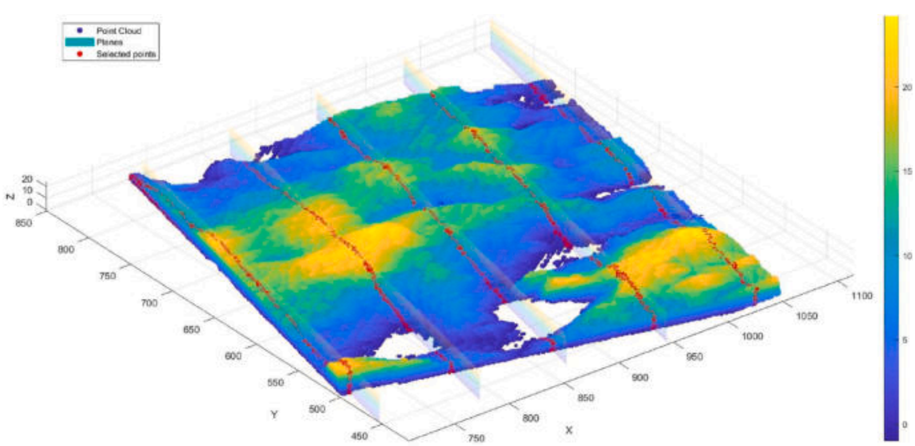

Fig. 4. Method used to extract roughness profiles, based on the extrapolation of five planes spaced 5 mm apart on the original point cloud.

intervals across the surface, as shown in Fig. 4, and each was used to extract a cross-sectional profile perpendicular to the local surface. These profiles were then used to detect surface roughness features by identifying local maxima and minima along the vertical axis. As reported in Fig. 4, some areas of the segmented fracture surfaces are characterized by missing data ("holes"). These zones can correspond either to real rock bridges, where the fracture is physically closed, or to artifacts introduced by the segmentation algorithm. As the aim of this work was to quantify the roughness of the open fracture surfaces, such areas were not analyzed further and were excluded from the roughness calculation. The orientation of roughness profiles was defined by convention as the direction of maximum slope of the mean fracture plane, relative to the core axis. All roughness values were therefore measured consistently with respect to this reference direction.

The roughness parameter R_z (Diaz et al., 2017) was calculated for each profile as,

$$R_z = \max(z) - \min(z) \tag{1}$$

To convert R_z into an estimate of the Joint Roughness Coefficient, two empirical models developed by (Li and Zhang, 2015) were applied,

$$\mathrm{JRC}E5 = 1.5715 \cdot R_z + 4.0318 \text{ for } R_z \in [0,\ 10.161],\ \mathrm{mm} \tag{2}$$

$$\mathrm{JRC}E6 = 4.4192 \cdot R^{0.6482} \text{ for } R_z \in [0,\ 10.269],\ \mathrm{mm} \tag{3}$$

We adopted the equation proposed by Li and Zhang (2015) for all roughness measurements, since it is independent of the sampling interval. This metric is commonly used in surface metrology as a reliable indicator of topographic variation. R_z was selected as the reference parameter because it allows for robust comparison across CT-derived, microscopy, and Barton comb datasets, and because of its established empirical correlation with JRC as demonstrated by Li and Zhang (2015). While more sophisticated descriptors such as Z_2 or fractal parameters are available, Rz offers the advantage of being independent of sampling interval and profile orientation. Its adequacy in this context is supported by the strong agreement between R_z-based JRC estimates and validation measurements. Future work will extend the methodology to incorporate alternative descriptors (e.g., Z_2) to capture additional morphological aspects of fracture roughness.

2.3. Experimental validation

In the experimental validation, two methods were employed to extract the JRC: (a) applying the CNN to the point cloud derived from high-resolution microscope data; and (b) calculation from the Barton comb profilometer extraction. The roughness measurements were performed on the same portions of the specimen to ensure the highest possible correspondence between the different measurement techniques. Although splitting the sample was necessary to expose the internal fracture surfaces for high-resolution microscopy and Barton comb measurements, this was done exclusively to validate the non-destructive CT-based workflow. Once validated, the proposed approach can be applied to intact core samples without any further destructive intervention. The combination of both digital and analog techniques thus strengthened the overall reliability of the results and supports the method's future application as a truly non-destructive tool for fracture roughness characterization.

2.3.1. Digital microscope for surface topography

A direct surface measurement using a high-resolution digital microscope was used as an experimental validation procedure. To perform the measurement, the rock sample was broken along the fracture, exposing the surface for analysis. The microscope used for this purpose offered variable magnification up to 2350X, a lateral resolution down to 0.4 μm, and depth resolution in the micrometer range, enabling accurate 3D surface characterization. The imaging system allowed for automatic stitching and height mapping, providing a detailed reconstruction of the fracture morphology. The measurement was carried out on the same surface portions used to calculate the JRC from 3D tomography data, such as F1 and F2-1 (Fig. 4), ensuring a direct correspondence between the numerical and experimental data. The roughness parameters were extracted using the same computational procedure applied to the tomographic point cloud data, allowing for a consistent and quantitative comparison between the two sources. These measurements served to validate the numerical roughness estimates, particularly in terms of amplitude and spatial frequency of surface irregularities.

2.3.2. Barton comb profilometer digitization

To further validate the obtained roughness parameters, complementary measurements were conducted using a mechanical profilometer based on Barton's methodology (Barton and Choubey, 1977). This method involves physically tracing the fracture surface with a Barton comb to capture its profile and derive roughness indices, such as the JRC. This established reference technique enabled direct comparison with the values computed through our digital workflow. To obtain a digitized version of the comb profile suitable for quantitative analysis, Barton's comb was first custom-made to match the surface to be analyzed, following the directions measured in the tomography. The comb was then scanned using a standard flatbed scanner at a resolution of 1448 × 2573 pixels, with a bright background to enhance contrast. The resulting images (Fig. 5) were processed using dedicated software developed in MATLAB. Each individual needle of the comb was identified, and both its diameter and position in pixels were measured. The diameter measurement was used to calibrate the image by comparing it with the known physical diameter of the needles (0.7 mm), allowing precise determination of the structural resolution of the profile reconstruction. The position of each needle was extracted across all pixels it covered, using a Gaussian convolution algorithm to filter noise and improve measurement accuracy. The extracted positions were then averaged to increase robustness. The algorithm allowed sub-pixel accuracy, conservatively estimated at 1/20 of a pixel. When combined with the scanner resolution, this yields an overall spatial resolution of the analysis equal to 0.0389 mm/pixel. Given the low level of noise observed during digitization, the uncertainty in measurement can be reasonably considered equivalent to the resolution, i.e., 0.002 mm. From the reconstructed digital profile, topographic parameters were extracted and used to compute JRC estimators following the empirical formulas proposed by Li and Zhang (2015). This approach provided a reproducible, quantitative basis for evaluating surface roughness from the comb measurements, enabling a robust comparison with the results obtained through deep learning-based analysis.

3. Results and discussion

3.1. Fracture network extraction

The fracture network extracted using the CNN is shown in Fig. 6 as a point cloud representation. The resolution of the point cloud is 70.69 × 10−3 mm, corresponding to the tomography resolution. In many studies, the point cloud is meshed to fill gaps that arise either from limitations of the extraction algorithm itself or from the application of specific thresholds during processing (Diaz et al., 2017). Although many methods exist in the literature for generating meshes of fracture networks from point clouds, they are mostly applicable to simple fracture configurations (Sun et al., 2013; Mustapha et al., 2011). In our case, the discontinuities are non-planar fractures. For this reason, the authors argue that, when calculating surface roughness, it is preferable to avoid introducing artifacts that may distort complex geometries. As reported by Sun et al. (2013), the effectiveness of meshing-based approaches often depends on the quality of discretization, which becomes particularly critical when working with intricate three-dimensional surfaces. In the proposed method, no thresholding is applied, allowing the original resolution and morphology of the fracture surfaces to be fully preserved. As shown by the fracture network, two main discontinuities cross the specimen with an inclination of approximately 70° with respect to the horizontal. These two discontinuities intersect each other, as shown in Fig. 6. As evident from the figure, the discontinuities in this specimen are characterized by non-planarity; they exhibit significant variation in dip direction along the specimen. The roughness calculation will therefore be performed on both discontinuities, hereafter referred to as Clusters 1 and 2 (Fig. 6). It should be noted that the proposed CNN-based workflow is fundamentally based on detecting contrasts between the rock matrix and discontinuities. Therefore, although this study focuses

Fig. 5. Scanned image of the Barton comb used for roughness quantification. The individual teeth were identified and processed to reconstruct the profile, enabling calibration based on tooth diameter (0.7 mm) and achieving a vertical resolution of 0.04 mm.

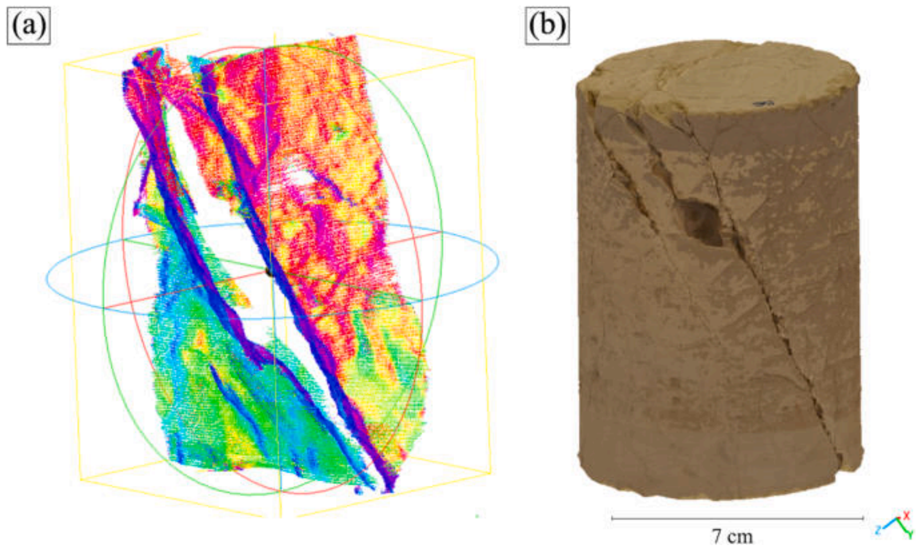

Fig. 6. (a) 3D fracture network extracted from CT data; (b) rock core sample.

on the sample analyzed, the method can be easily adapted and scaled to other rock types, provided that the contrast between the fractures and the surrounding matrix is sufficient for the extraction of reliable features.

3.2. Uncertainty in fracture network extraction

The reconstruction of fracture networks from volumetric imaging data is inherently affected by uncertainty, due both to the geometric complexity of natural fractures and the limitations of current extraction techniques. Rock discontinuities often exhibit irregular shapes, branching structures, and varying degrees of mineral infill, all of which complicate their detection in CT images. In particular, spatial resolution and imaging noise can significantly impact the quantification of key fracture attributes, such as surface area and porosity (McBeck et al., 2021). Even small variations in voxel intensity may lead to misinterpretation of discontinuity extents, especially in the case of narrow or low-contrast features. Deterministic extraction methods, based on voxel intensity gradients and local minima, are commonly employed to highlight open discontinuities (Deng et al., 2016). These approaches offer good noise suppression and geometric coherence, favoring accuracy by minimizing false positives. However, this comes at the cost of completeness: subtle or poorly defined features are often excluded, resulting in partial reconstruction of complex fracture networks and thus introducing uncertainty into their spatial characterization (Deng et al., 2016). A key innovation of our approach lies in the training strategy of the CNN, which was developed using a curated dataset of manually labeled fractures. This supervised learning framework enables the network to learn spatial patterns and recognize morphologically complex or low-contrast features that traditional image analysis techniques might fail to capture (Lei and Fan, 2024). As a result, the extracted fracture networks exhibit improved continuity and completeness. This outcome reflects the strength of our curated and diverse dataset, which included 750 images from open-source sources and internal EU project data, used to train, validate, and test the U-Net architecture (Caputo et al., 2025).

Crucially, the successful application of a model trained primarily on structural defects to geological samples confirms the hypothesis that morphological features of fractures share universal characteristics across domains. This cross-domain robustness validates the proposed workflow as a generalized tool, capable of operating without the need for extensive, site-specific geological training datasets often required by other deep learning approaches. The model loss was computed as the sum of Dice loss and focal loss, and the training was performed over 130 epochs (Caputo et al., 2025). Nevertheless, deep learning approaches have their own limitations. Misclassifications at the voxel scale can introduce artifacts such as oversegmentation, the inclusion of non-fracture elements, or discontinuities where fractures are not fully identified. However, some features are not missing due to CNN limitations, but rather due to the intrinsic limitations of the tomographic data itself. Specifically, stylolites and calcite-filled veins—despite being composed of the same material as the host rock—are not clearly visible in CT images. Stylolites are often thinner than the spatial resolution of the scan, and sealed veins made of calcite exhibit X-ray attenuation values nearly identical to the surrounding carbonate matrix, making them fundamentally undetectable even before any machine learning processing takes place (Christe et al., 2007; Ketcham et al., 2010). As reported by Christe et al. (2007), fracturing of limestones under tectonic processes involves the circulation of calcite-rich fluids, which preferentially precipitate within open cracks and progressively seal the fractures, altering their mechanical properties. Due to the similar densities of the precipitated calcite and the limestone matrix, these sealed features often become undetectable in CT scans. Considering the inherent limitations of CT imaging and the quality of the input data, our model has nonetheless demonstrated a strong ability to identify very thin open fractures, which are visible due to the high attenuation contrast created by voids or air-filled gaps, as evidenced by Caputo et al. (2025).

3.3. Roughness calculation and validation

Table 1 presents the roughness parameters derived from the elaboration of CT data and high-resolution optical microscope acquisitions for the joint surfaces identified by the CNN (J1 and J2 in Fig. 8a and b). To ensure consistency and comparability between the two acquisition techniques, the roughness parameters were calculated over the same nominal surface areas. These regions, highlighted in the corresponding figures, were carefully selected to correspond spatially across the CT and microscope datasets. However, due to the nature of the test procedure, the microscope-based measurements were performed after specimen failure, and thus analyzed a portion of the actual fractured surface. This may have introduced minor discrepancies in sampling shape and extent, though the spatial alignment with the CT regions was preserved. Representative high-resolution images of the microscope-acquired surfaces are shown in Fig. 7, highlighting the detail level and surface morphology captured after specimen failure.

As shown in Table 1, surface J1-1 was further subdivided into two

Table 1
Comparison of roughness parameters extracted from 5 planes for each joint and from CT and high-resolution microscope. Average JRC values for each joint are reported.

Method	Joint ID	Plane	Z_{min} (mm)	Z_{max} (mm)	R_z (mm)	JRC			
						*E*5	*E*5 Avg	*E*6	*E*6 Avg
CT	J1-1	1	−0.1	1.3	1.3	6.1	6.6	5.4	6.0
		2	−0.1	1.8	1.9	6.9		6.6	
		3	−0.1	1.3	1.4	6.2		5.4	
		4	−0.1	1.4	1.5	6.4		5.7	
		5	−0.1	2.0	2.0	7.2		7.0	
	J1-2	1	−0.1	1.5	1.6	6.5	6.5	5.9	5.9
		2	−0.1	1.6	1.7	6.6		6.1	
		3	−0.1	1.2	1.3	6.1		5.3	
		4	−0.1	1.5	1.6	6.5		5.9	
		5	−0.1	1.6	1.7	6.6		6.1	
	J2	1	−0.1	1.5	1.6	6.5	6.5	5.9	5.9
		2	−0.1	1.6	1.7	6.6		6.1	
		3	−0.1	1.2	1.3	6.1		5.3	
		4	−0.1	1.5	1.6	6.5		5.9	
		5	−0.1	1.6	1.7	6.6		6.1	
High resolution microscope	J1-1	1	−1.0	0.2	1.2	6.0	7.3	5.07	7.1
		2	−1.0	1.3	2.3	7.6		7.49	
		3	−1.0	1.3	2.3	7.7		7.68	
		4	−1.0	1.6	2.6	8.1		8.15	
		5	−1.0	1.1	2.1	7.4		7.23	
	J1-2	1	−0.9	0.9	1.8	6.9	6.3	6.6	5.5
		2	−0.3	0.4	0.6	5.0		3.3	
		3	−0.7	1.2	1.8	6.9		6.5	
		4	−0.5	0.7	1.3	6.1		5.2	
		5	−1.0	0.6	1.6	6.6		6.0	
Barton comb	J1-1		0.2	2.5	2.3		7.7		7.7
	J1-2		1.8	3.5	1.6		6.6		6.1

sub-regions (J1-1 and J1-2) for a more detailed analysis. An overview of plane extraction for each surface is shown in Fig. 8c (CT-derived point cloud) and Fig. 8d (microscope-derived point cloud). The evaluated parameters include the vertical range of the surface (Z_{min} and Z_{max}), the maximum height roughness parameter (R_z), and the estimated JRC based on the empirical models (E5 and E6, Li and Zhang (2015)). The values of E5 and E6 are presented individually for each plane, along with their joint-averaged values. CT-derived JRC values exhibit strong consistency with those obtained from the high-resolution microscope, especially when considering the average estimators. For instance, for joint J1-1, the average JRC values from CT are 6.6 (E5) and 6.0 (E6), while the corresponding microscope-derived values are 7.3 (E5) and 7.1 (E6). Similarly, for joint J1-2, CT yields average JRCs of 6.5 (E5) and 5.9 (E6), compared to 6.3 (E5) and 5.5 (E6) from the microscope. These differences, generally within 1 to 1.5 JRC units, reflect a high level of agreement considering the distinct acquisition methods and surface conditions.

The R_z parameter also supports this comparison: although microscope values tend to be slightly higher—due to finer detection of post-failure micro-asperities—the overall range remains consistent with CT-based measurements.

According to the reference profiles defined by Barton and Choubey (1977), JRC values in the range of 5–8 correspond to moderately rough surfaces, typically featuring small steps or gentle undulations. The values obtained through both CT and microscope methods fall within this interval, confirming that the classification remains stable regardless of technique. The small discrepancies are attributed to acquisition conditions (e.g., post-fracture alterations, resolution differences) and do not significantly affect the interpretation of the mechanical behavior associated with joint roughness.

The digitization of the Barton comb enabled further validation of roughness quantification methods (Table 1). Although this traditional technique is limited in resolution compared to modern digital methods, it remains a widely accepted reference in the field (Tatone and Grasselli, 2010; Yong et al., 2018). For example, Barton comb estimates yielded average JRC values of 7.7 (J1-1) and 6.6/6.1 (J1-2, E5/E6), which are in line with those obtained from CT and microscope data. Recent developments, such as the use of vector similarity measures for JRC

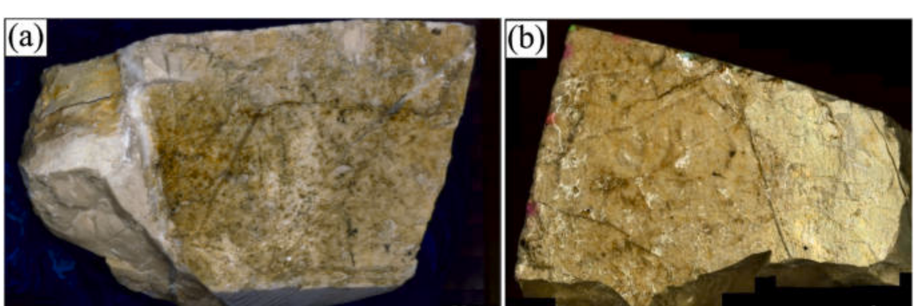

Fig. 7. High-resolution optical microscope images of fracture surfaces (a) J1-1 and (b) J1-2.

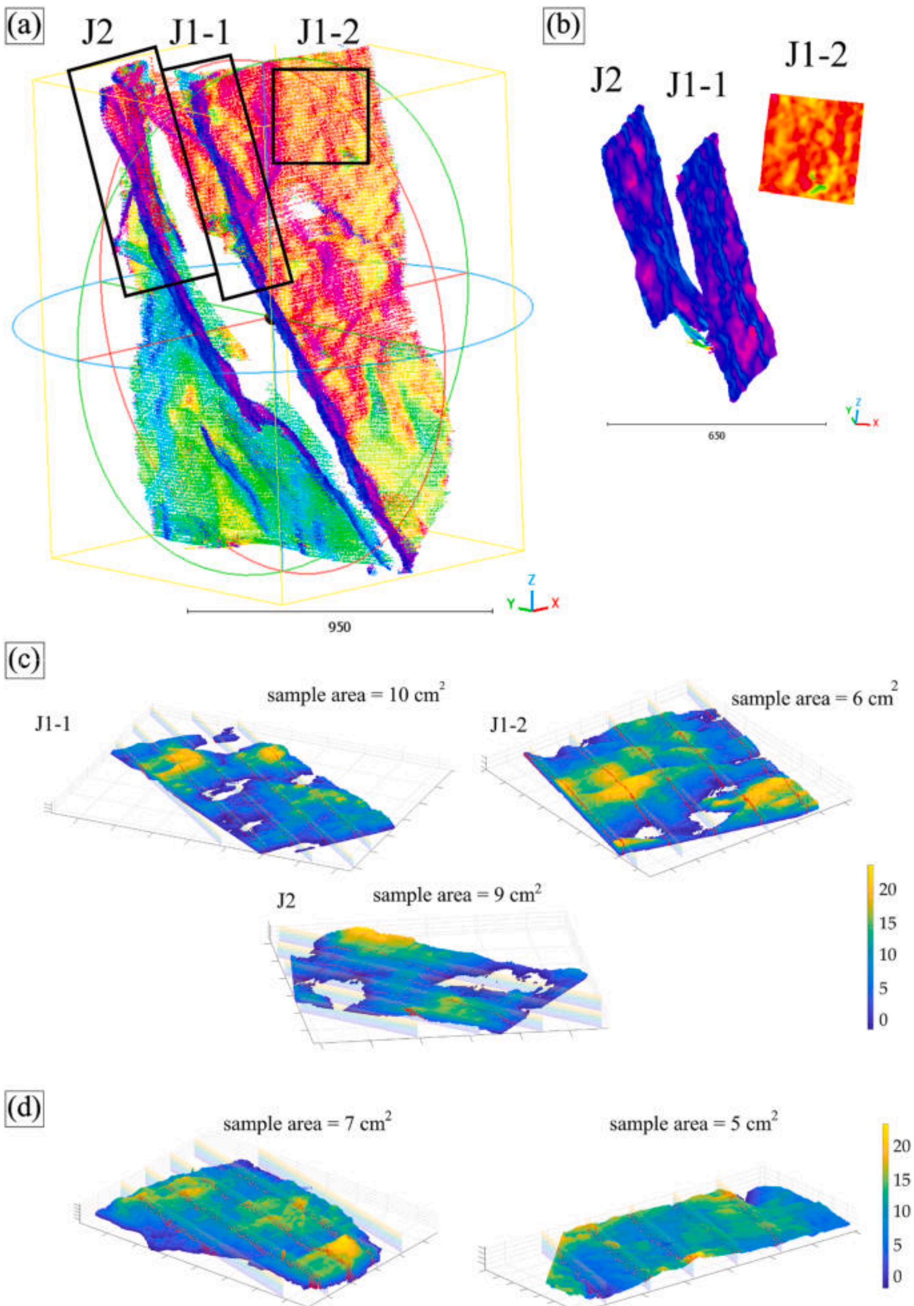

Fig. 8. Roughness analysis from CT and high-resolution microscopy. (a) 3D rendering of CT point cloud showing joint surfaces J1-1, J1-2, and J2. (b) Corresponding high-resolution microscope views. (c–d) Roughness sampling areas on CT (c) and microscope (d) point clouds.

estimation, underscore the increasing accuracy and reproducibility of digital approaches (Yong et al., 2018). These results confirm that the CT-based method offers a robust and reliable non-destructive solution for fracture roughness assessment, particularly when post-failure access is limited (Cnudde and Boone, 2013). This consistency across methods indicates that the CT-based workflow, while operating at laboratory resolution, yields JRC values directly comparable with those obtained by field techniques such as the Barton comb, thereby bridging the gap between laboratory-scale measurements and engineering-scale applications. Despite the segmentation challenges discussed above, the proposed workflow provides consistent and engineering-relevant estimates of fracture roughness. The CT-derived JRC values are compatible with established models such as Barton-Bandis (Barton et al., 1985) while the non-destructive and automated nature of the method enables scalable analysis of internal joints. These aspects extend its practical applicability to key geotechnical domains such as tunneling, slope stability, and reservoir characterization.

3.4. Uncertainty in roughness determination

The current study presents a novel deep learning-based workflow that first segments fracture networks from X-ray CT data using a CNN, and then computes the JRC from the resulting fracture point clouds. The performance and reliability of this integrated, non-destructive digital approach are rigorously evaluated through direct comparison of the obtained JRC values with those derived from established reference methods: point clouds generated from high-resolution digital microscope images and digitized profiles acquired with the Barton comb. This multi-method validation is crucial, as the inherent disparities in measurement scale and resolution between these techniques mean that each method samples roughness information at distinct levels of detail, underscoring the challenge of defining the “ground truth” (Barton and Choubey, 1977; Xie et al., 1997). By demonstrating strong agreement between the CT-based results and both reference methods (Table 1), this work provides valuable insights into the reliability and robustness of the proposed approach, offering a more objective and comprehensive characterization of fracture roughness despite the inherent uncertainties of its determination. It should also be noted that JRC is inherently anisotropic and heterogeneous, and simplified descriptors such as R_z cannot capture the full directional dependence of surface roughness. In this study, this limitation was mitigated by sampling multiple profiles across each fracture surface, thereby accounting for variability, and by validating CT-derived values against microscopy and Barton comb measurements. The strong agreement obtained supports the adequacy of the chosen metric for our objectives, although future work will integrate orientation-dependent descriptors to explicitly address anisotropy.

It is important to note that the optical microscope measurements required intentional failure of the core sample to physically expose the fracture surfaces. This was done through controlled uniaxial splitting along the main discontinuity plane. Although this approach ensures that the same fracture identified by CT could be directly measured, the induced breakage may introduce micro-asperities, chipping, or small-scale roughness features that do not exist in the intact rock. Such post-failure modifications can locally increase the measured R_z and hence bias the estimated JRC slightly higher than the CT-based values, which represent the internal geometry prior to failure. This possible source of discrepancy is partially mitigated by averaging over multiple profiles and by comparing with the Barton comb results, but should be considered when interpreting the validation. Moreover, techniques relying on the Barton comb or other digitized 2D profiles are often susceptible to operator dependency and suffer from inherent constraints in resolution and scale representativeness. The reduction of a complex 3D phenomenon to 2D profiles fundamentally discards information, while the discrete nature of data acquisition may fail to capture crucial micro-asperities. Similarly, optical and photogrammetric techniques, though offering non-contact solutions, are sensitive to illumination conditions, sensor resolution, and the accuracy of 3D point cloud reconstruction. Even minor errors in image acquisition or processing can propagate into the final roughness quantification. Furthermore, the specific algorithms employed to convert these point clouds into JRC values can introduce additional variability. It is worth noting that, although CT and microscopy capture small-scale asperities, their negligible impact at engineering scales is confirmed by the strong agreement with Barton comb measurements, which remain representative of field practice.

In this regard, it should be noted that the empirical conversion from R_z to JRC in this work relies on the Li and Zhang (2015) relationships, which were chosen for their suitability for height-based descriptors and CT-derived point clouds. While other empirical models were considered, they were not applicable to our data format, but it is acknowledged that different formulas may produce slight variations in JRC, adding to the overall uncertainty.

4. Conclusions

This study demonstrates a novel, fully digital workflow to quantitatively assess rock joint roughness using X-ray computed tomography combined with deep learning-based fracture segmentation. The method enables accurate extraction of internal discontinuities as high-resolution 3D point clouds and computes surface roughness parameters, converting R_z to JRC through empirical relations by Li and Zhang (2015). Validation against high-resolution optical microscopy and digitized Barton comb profiles show that CT-derived JRC values agree well with conventional reference measurements, confirming the robustness of the non-destructive approach. Key sources of uncertainty, such as segmentation limitations, post-failure surface changes, and the choice of empirical conversion, have been critically discussed. The results highlight that the method provides realistic input parameters for estimating shear strength in geomechanical models. Overall, the proposed integration of CT-based 3D modeling and machine learning offers a robust tool to bridge laboratory-scale roughness evaluation and field-scale rock mechanics practice.

CRediT authorship contribution statement

Elisa Mammoliti: Writing – original draft, Validation, Supervision, Software, Project administration, Methodology, Investigation, Data curation, Conceptualization. **Alessia Caputo:** Writing – original draft, Validation, Software, Investigation, Data curation, Conceptualization. **Maria Teresa Calcagni:** Writing – original draft, Software, Investigation, Data curation, Conceptualization. **Giovanni Salerno:** Writing – original draft, Software, Investigation, Data curation, Conceptualization. **Paolo Castellini:** Writing – review & editing, Supervision, Software, Project administration, Methodology, Formal analysis, Data curation, Conceptualization.

Declaration of competing interest

The authors declare that they have no known competing financial interests or personal relationships that could have appeared to influence the work reported in this paper.

References

Alzubaidi, F., Mostaghimi, P., Swietojanski, P., Clark, S.R., Armstrong, R.T., 2021. Automated lithology classification from drill core images using convolutional neural networks. J. Petrol. Sci. Eng. 197, 107933.
Alzubaidi, F., Nalinakumar, H., Clark, S.R., Lie, J.E., Mostaghimi, P., Armstrong, R.T., 2023. Improved fracture segmentation from un-wrapped drill-core images using an innovative two-stage segmentation approach. Math. Geosci. 55, 829–857.
Barton, N., Bandis, S., Bakhtar, K., 1985. Strength, deformation and conductivity coupling of rock joints. Int. J. Rock Mech. Min. Sci. Geomech. Abstr. 22, 121–140.
Barton, N., Choubey, V., 1977. The shear strength of rock joints in theory and practice. Rock Mech. 10, 1–54.
Bieniawski, Z., Hawkes, I., 1978. Suggested methods for determining tensile strength of rock materials. Int. J. Rock Mech. Min. Sci. 15, 99–103.
Bons, P.D., 2000. The formation of veins and their microstructures. J. Virtual Explor. 2 (2).
Brady, B.H., Brown, E.T., 2006. Rock Mechanics: For Underground Mining. Springer Science & Business Media.
Brown, S.R., Kranz, R.L., Bonner, B.P., 1986. Correlation between the surfaces of natural rock joints. Geophys. Res. Lett. 13, 1430–1433.
Calamita, F., Deiana, G., 1986. Evoluzione strutturale neogenico-quaternaria dell’appennino umbro-marchigiano. In Studi Geologici Camerti. Nuova Serie , pp. 91–98.
Calcagni, M.T., Salerno, G., Martarelli, M., Schlenger, J.U., Hassan, T., Heinikainen, R., Borrmann, A., Fies, B., Revel, G.M., 2025. Concrete defect identification and measurement in buildings. Acta IMEKO 14, 1–11.
Caputo, A., Calcagni, M.T., Salerno, G., Mammoliti, E., Castellini, P., 2025. Measurement of fracture networks in rock sample by X-ray tomography, convolutional filtering and deep learning. Sensors 25, 4409.
Cello, G., Mazzoli, S., Tondi, E., Turco, E., 1997. Active tectonics in the central apennines and possible implications for seismic hazard analysis in peninsular Italy. Tectonophysics 272, 43–68.
Centamore, E., Chiocchini, M., Deiana, G., Micarelli, A., Pieruccini, U., 1971. Contributo alla conoscenza del giurassico dell’appennino umbro-marchigiano. Stud. Geol. Camerti 1, 7–89.
Chen, J., Zhou, M., Huang, H., Zhang, D., Peng, Z., 2021. Automated extraction and evaluation of fracture trace maps from rock tunnel face images via deep learning. Int. J. Rock Mech. Min. Sci. 142, 104745.
Chen, L., Chen, W., Wang, L., Zhai, C., Hu, X., Sun, L., Tian, Y., Huang, X., Jiang, L., 2023. Convolutional neural networks (CNNs)-based multi- category damage detection and recognition of high-speed rail (HSR) reinforced concrete (RC) bridges using test images. Eng. Struct. 276, 115306.
Chiffre, L.D., Carmignato, S., Kruth, J.P., Schmitt, R., Weckenmann, A., 2014. Industrial applications of computed tomography. CIRP Ann. 63, 655–677.
Christe, P., Bernasconi, M., Vontobel, P., Turberg, P., Parriaux, A., 2007. Three-dimensional petrographical investigations on borehole rock samples: a comparison between X-ray computed-and neutron tomography. Acta Geotech. 2, 269–279.
Cnudde, V., Boone, M.N., 2013. High-resolution X-ray computed tomography in geosciences: a review of the current technology and applications. Earth Sci. Rev. 123, 1–17.
Deiana, G., Pialli, G., 1994. The structural provinces of the umbro-marchean apennines. Memor. Soc. Geol. Ital. 48, 473–484.

Deng, H., Fitts, J.P., Peters, C.A., 2016. Quantifying fracture geometry with X-ray tomography: technique of iterative local thresholding (TILT) for 3D image segmentation. Comput. Geosci. 20, 231–244.

Diaz, M., Kim, K.Y., Yeom, S., Zhuang, L., Park, S., Min, K.B., 2017. Surface roughness characterization of open and closed rock joints in deep cores using X-ray computed tomography. Int. J. Rock Mech. Min. Sci. 98, 10–19.

Ge, Y., Kulatilake, P.H., Tang, H., Xiong, C., 2014. Investigation of natural rock joint roughness. Comput. Geotech. 55, 290–305.

Giulietti, N., Caputo, A., Chiariotti, P., Castellini, P., 2023. Swimmernet: underwater 2D swimmer pose estimation exploiting fully convolutional neural networks. Sensors 23, 2364.

Guo, Y., Liu, D., Li, J., Liu, J., Tong, X., 2025. A logistic-based constitutive model for rocks under uniaxial compression considering the initial damage recovery characteristics. Rock Mech. Bull., 100216.

Glover, P., Matsuki, K., Hikima, R., Hayashi, K., 1998. Fluid flow in synthetic rough fractures and application to the hachimantai geothermal hot dry rock test site. J. Geophys. Res. Solid Earth 103, 9621–9635.

Gmb, C.Z.U.I.M., 2015. METROTOM OS user software for CT scanners. Operating Instructions. D-73446 Oberkochen.

International Organization for Standardization. ISO 16371-2:2017: Non-destructive testing — Industrial computed radiography with storage phosphor imaging plates — Part 2: General principles for testing of metallic materials using X-rays and gamma rays. https://www.iso.org/standard/67690.html.

International Society for Rock Mechanics, 1981. Rock Characterization Testing & Monitoring: ISRM Suggested Methods. Pergamon Press.

Invernizzi, M.C., 1994. Low temperature deformation in naturally deformed marly limestones from the Umbria-Marche Apennines (central Italy). Annales Tectonicae 8, 119–133 (2).

Ketcham, R.A., 2006. Accurate three-dimensional measurements of features in geological materials from X-ray computed tomography data. Adv. X-ray Tomography Geomater. 143–148.

Ketcham, R.A., Carlson, W.D., 2001. Acquisition, optimization and interpretation of X-ray computed tomographic imagery: applications to the geosciences. Comput. Geosci. 27, 381–400.

Ketcham, R.A., Slottke, D.T., Sharp Jr, J.M., 2010. Three-dimensional measurement of fractures in heterogeneous materials using high-resolution X-ray computed tomography. Geosphere 6, 499–514.

Kruth, J., Bartscher, M., Carmignato, S., Schmitt, R., Chiffre, L.D., Weckenmann, A., 2011. Computed tomography for dimensional metrology. CIRP Ann. 60, 821–842.

Lei, J., Fan, Y., 2024. Rock CT image fracture segmentation based on convolutional neural networks. Rock Mech. Rock Eng. 57, 5883–5898.

Li, Y., Zhang, Y., 2015. Quantitative estimation of joint roughness coefficient using statistical parameters. Eng. Geol. 187, 91–103.

López-Torres, C.V., Salazar Colores, S., Kells, K., Pedraza-Ortega, J.C., Ramos-Arreguin, J.M., 2020. Improving 3D reconstruction accuracy in wavelet transform profilometry by reducing shadow effects. IET Image Process. 14, 310–317.

Marchegiani, L., Bertotti, G., Cello, G., Deiana, G., Mazzoli, S., Tondi, E., 1999. Pre-orogenic tectonics in the Umbria–Marche sector of the Afro-Adriatic continental margin. Tectonophysics 315, 123–143.

McBeck, J.A., Cordonnier, B., Renard, F., 2021. The influence of spatial resolution and noise on fracture network properties calculated from X-ray microtomography data. Int. J. Rock Mech. Min. Sci. 147, 104922.

Mustapha, H., Dimitrakopoulos, R., Graf, T., Firoozabadi, A., 2011. An efficient method for discretizing 3D fractured media for subsurface flow and transport simulations. Int. J. Numer. Methods Fluid. 67, 651–670.

Pham, C., Zhuang, L., Yeom, S., Shin, H.S., 2023. Automatic fracture characterization in CT images of rocks using an ensemble deep learning approach. Int. J. Rock Mech. Min. Sci. 170, 105531.

Ronneberger, O., Fischer, P., Brox, T., 2015. U-net: convolutional networks for biomedical image segmentation. In: Medical Image Computing and computer-assisted intervention–MICCAI 2015: 18th International Conference, Munich, Germany, October 5-9, 2015, Proceedings, Part III 18. Springer, pp. 234–241.

Salerno, G., Calcagni, M.T., Martarelli, M., Revel, G.M., 2024. Metrological evaluation of an AI-based vision computing model for crack detection on masonry structures. In: MATEC Web of Conferences. In: EDP Sciences p.04002.

Salvini, R., Vanneschi, C., Coggan, J.S., Mastrorocco, G., 2020. Evaluation of the use of UAV photogrammetry for rock discontinuity roughness characterization. Rock Mech. Rock Eng. 53, 3699–3720.

Sun, S., Sui, J., Chen, B., Yuan, M., 2013. An efficient mesh generation method for fractured network system based on dynamic grid deformation. Math. Probl. Eng. 2013, 834908.

Tatone, B.S., Grasselli, G., 2010. A new 2D discontinuity roughness parameter and its correlation with JRC. Int. J. Rock Mech. Min. Sci. 47, 1391–1400.

Tian, Y., Wang, D., Xia, J., Ma, Y., Zhang, Y., Li, B., Ding, H., 2025. Digital rock modeling of deformed multi-scale media in deep hydrocarbon reservoirs based on in-situ stress-loading CT imaging and U-Net deep learning. Mar. Petrol. Geol. 171, 107177.

Tse, R., Cruden, D., 1979. Estimating joint roughness coefficients. Int. J. Rock Mech. Min. Sci. Geomech. Abstr. 16 (5), 303–307.

Vu, M., Jardani, A., 2022. Mapping discrete fracture networks using inversion of hydraulic tomography data with convolutional neural network: Segnet-fracture. J. Hydrol. 609, 127752.

Xie, H., Wang, J.A., Kwaśniewski, M., 1999. Multifractal characterization of rock fracture surfaces. Int. J. Rock Mech. Min. Sci. 36, 19–27.

Xie, H., Wang, J.A., Xie, W.H., 1997. Fractal effects of surface roughness on the mechanical behavior of rock joints. Chaos Solitons Fractals 8, 221–252.

Yaqoob, M., Ishaq, M., Ansari, M.Y., Konagandla, V.R.S., Tamimi, T.A., Tavani, S., Corradetti, A., Seers, T.D., 2024. Geocrack: a high-resolution dataset for segmentation of fracture edges in geological outcrops. Sci. Data 11.

Yong, R., Ye, J., Liang, Q.F., Huang, M., Du, S.G., 2018. Estimation of the joint roughness coefficient (JRC) of rock joints by vector similarity measures. Bull. Eng. Geol. Environ. 77, 735–749.

Zvarivadza, T., Lawal, A.I., Onifade, M., Mulenga, F., Kwon, S., Khandelwal, M., 2025. Deep learning-powered rock mass classification: predicting RMR from Q-System parameters with high accuracy. Rock Mech. Bull. 4 (4), 100219.